

## NATURE OF W51E2: MASSIVE CORES AT DIFFERENT PHASES OF STAR FORMATION

HUI SHI<sup>1</sup>, JUN-HUI ZHAO<sup>2</sup>, J.L. HAN<sup>1</sup>,  
*Draft version October 30, 2018*

### ABSTRACT

We present high-resolution continuum images of the W51e2 complex processed from archival data of the Submillimeter Array (SMA) at 0.85 and 1.3 mm and the Very Large Array at 7 and 13 mm. We also made line images and profiles of W51e2 for three hydrogen radio recombination lines (RRLs; H26 $\alpha$ , H53 $\alpha$ , and H66 $\alpha$ ) and absorption of two molecular lines of HCN(4-3) and CO(2-1). At least four distinct continuum components have been detected in the 3'' region of W51e2 from the SMA continuum images at 0.85 and 1.3 mm with resolutions of 0.3''  $\times$  0.2'' and 1.4''  $\times$  0.7'', respectively. The west component, W51e2-W, coincides with the ultracompact HII region reported from previous radio observations. The H26 $\alpha$  line observation reveals an unresolved hyper-compact ionized core ( $< 0.06''$  or  $< 310$  AU) with a high electron temperature of  $1.2 \times 10^4$  K, with the corresponding emission measure  $EM > 7 \times 10^{10}$  pc cm<sup>-6</sup> and the electron density  $N_e > 7 \times 10^6$  cm<sup>-3</sup>. The inferred Lyman continuum flux implies that the HII region W51e2-W requires a newly formed massive star, an O8 star or a cluster of B-type stars, to maintain the ionization. W51e2-E, the brightest component at 0.85 mm, is located 0.9'' east from the hyper-compact ionized core. It has a total mass of  $\sim 140 M_\odot$  according to our spectral energy distribution analysis and a large infall rate of  $> 1.3 \times 10^{-3} M_\odot \text{yr}^{-1}$  inferred from the absorption of HCN. W51e2-E appears to be the accretion center in W51e2. Given the fact that no free-free emission and no RRLs have been detected, the massive core of W51e2-E appears to host one or more growing massive proto-stars. Located 2'' northwest from W51e2-E, W51e2-NW is detected in the continuum emission at 0.85 and 1.3 mm. No continuum emission has been detected at  $\lambda \geq 7$  mm. Along with the maser activities previously observed, our analysis suggests that W51e2-NW is at an earlier phase of star formation. W51e2-N is located 2'' north of W51e2-E and has only been detected at 1.3 mm with a lower angular resolution ( $\sim 1''$ ), suggesting that it is a primordial, massive gas clump in the W51e2 complex.

*Subject headings:* HII regions – ISM: individual objects (W51e2) – stars: formation

### 1. INTRODUCTION

Massive stars are formed in dense, massive molecular cores. Detailed physical processes in star-forming regions have not been well studied until recent high-resolution observations were available at submillimeter wavelengths. High angular resolution observations are necessary to unveil the physical environs and activities of the individual sub-cores as well as their impact on the overall process of massive star formation.

W51 is a well-known complex of HII regions with about 1° area in the Galactic plane (Westerhout 1958). W51A, also called G49.5-0.4, is the most luminous region in W51 (Kundu & Velusamy 1967). Several discrete components have been found from W51A and referred alphabetically as a–i in the right ascension (R.A.) order (Martin 1972; Mehringer 1994). W51e is one of the brightest regions in W51A. High-resolution centimeter observations have revealed that W51e consists of several ultracompact (UC) HII regions (Scott 1978; Gaume et al. 1993), among which the UC HII region of W51e2 appears to be the brightest. This region is severely obscured by the dust, and no IR detection has been made at wavelengths shorter than 20  $\mu$ m (Genzel et al. 1982). The inferred distance to W51e2 is  $\sim 5.1$  kpc (Xu et al. 2009); thus, 1'' corresponds to a linear scale of about 5100 AU.

Based on the radio continuum observations, spectral energy distribution (SED) analyses of W51e2 suggest that the emission source from this region consists of two components, namely, (1) thermal emission from a cold dust component and (2) free-free emission from a hot HII region (Rudolph et al. 1990; Sollins et al.

2004; Keto et al. 2008).

Observations of hydrogen radio recombination lines (RRLs) were carried out toward W51e2 (Mehringer 1994; Keto et al. 2008; Keto & Klaassen 2008). Mehringer (1994) failed to detect the H92 $\alpha$  line in this region, which might be attributed to the large optical depth and/or the large pressure broadening of the UC HII region at 3.6 cm. Based on the observations of H66 $\alpha$ , H53 $\alpha$ , and H30 $\alpha$ , Keto et al. (2008) argued that the pressure broadening is responsible for the broad-line widths observed in the RRLs.

Observations of molecular lines (e.g. Ho & Young 1996; Zhang & Ho 1997; Zhang et al. 1998; Young et al. 1998; Sollins et al. 2004) showed evidence for infall (or accretion) gas within 5'' ( $< 0.2$  pc) around W51e2. A possible rotation was suggested by Zhang & Ho (1997) on the basis of fitting the position–velocity (PV) diagram of the NH<sub>3</sub>(3,3) absorption line at 13 mm. A spin-up rotation with an axis of position angle (P.A.)  $\approx 20^\circ$  was further suggested based on the velocity gradient of CH<sub>3</sub>CN(8<sub>3</sub>–7<sub>3</sub>) at 2 mm (Zhang et al. 1998). However, based on the velocity gradient observed from the H53 $\alpha$  line, Keto & Klaassen (2008) interpreted their results as evidence for rotational ionized accretion flow around the UC HII region and derived a rotational axis of P.A.  $\approx -30^\circ$ . In addition, a possible bipolar outflow along the northwest and southeast (NW–SE) directions was suggested based on the observations of the CO(2-1) line emission (Keto & Klaassen 2008), which appears to be perpendicular to the axis of the rotational ionized disk. However, the southwest (SW) elongation of the UC HII region in Gaume et al.'s (1993) observations was explained as a collimated ionized outflow. On the other hand, proper-motion measurements of H<sub>2</sub>O/OH masers appeared to favor a hypothetical model with an outflow or expanding gas bubble in W51e2 (Imai et al. 2002; Fish & Reid 2007).

Thus, improved images and comprehensive analysis of high-

<sup>1</sup> National Astronomical Observatories, Chinese Academy of Sciences, Jia20 Datun Road, Chaoyang District, Beijing 100012, China. Email: shihui, hjl @ nao.cas.cn

<sup>2</sup> Harvard-Smithsonian Center for Astrophysics, 60 Garden Street, Cambridge, MA 02138, USA. Email: jzhao @ cfa.harvard.edu

TABLE 1  
OBSERVATION PARAMETERS FOR W51E2

Parameters	SMA: 0.85 mm	SMA: 1.3 mm	VLA: 7 mm	VLA: 13 mm
Observation date	2007 Jun. 18	2005 Sep. 1	2004 Feb. 14	2003 Sep. 29
Array configuration	Very extended (8 ants)	Extended (6 ants)	AB	BC
Pointing center R.A.(J2000)	19:23:43.888	19:23:43.895	19:23:43.918	19:23:43.918
Pointing center decl.(J2000)	+14:30:34.798	+14:30:34.798	+14:30:28.164	+14:30:28.164
Frequency(GHz)	343, 353	221, 231	43	22
Bandwidth	2.0+2.0 (GHz)	2.0+2.0 (GHz)	12.5 (MHz)	12.5 (MHz)
On-source time (hr)	2.10	4.75	5.90	3.93
System temperature(K)	150~500	100~250		
Bandpass calibrators	J1229+020, J1751+096	3C 454.4	3C 84	3C 84
Phase calibrators	J1733-130, J1743-038	J1751+096, J2025+337	J1923+210	J1923+210
	J2015+371			
Flux calibrators	Callisto	Ceres	3C 286	3C 286

resolution observations at the wavelengths from radio to sub-millimeter are needed to reconcile the differences in the interpretation of the results from the previous observations of W51e2. In this paper, we show the high-resolution continuum images with the Submillimeter Array (SMA) at 0.85 and 1.3 mm and with the Very Large Array (VLA) at 7 and 13 mm, as well as line images and profiles of the hydrogen recombination lines ( $H26\alpha$ ,  $H53\alpha$ , and  $H66\alpha$ ) and the molecular lines of HCN(4-3) and CO(2-1). In Section 2, we describe the details of the data processing and results. In Section 3, we model the individual components on the basis of the high-resolution observations of W51e2 with the SMA and VLA. The nature and astrophysical processes of star formation cores in W51e2 are discussed. A summary and conclusions are given in Section 4.

## 2. DATA REDUCTION AND RESULTS

We processed the archival data from the SMA and VLA observations of W51e2 and constructed both the continuum and spectral line images. Details in calibration and imaging are discussed below along with the relevant parameters that are summarized in Table 1.

### 2.1. The SMA continuum images at 0.85 and 1.3 mm

The observations of W51e2 at 0.85 mm were carried out with the SMA in the very extended array (eight antennas) and at 1.3 mm in the extended array (six antennas). The data were calibrated in Miriad (Sault et al. 1995) following the reduction instructions for SMA data<sup>3</sup>. The system temperature corrections were applied to the visibility data. The bandpass calibration was made with strong calibrators for each of the two data sets (Table 1). The flux density scale was determined using Callisto at 0.85 mm and Ceres at 1.3 mm.

Corrections to the complex gains at 1.3 mm were made by applying the solutions interpolated from the two nearby QSOs J1751+096 and J2025+337. For the high-resolution data at 0.85 mm, the visibility data are initially calibrated with a model of W51e2 derived from observations in a low angular resolution at 0.87 mm. The residual phase errors were further corrected using the self-calibration technique. The final continuum images were constructed by combining all the line-free channels in both upper sideband and lower sideband data.

Figure 1 shows the high-resolution ( $0.3'' \times 0.2''$ ) continuum image of W51e2 at 0.85 mm. The complex of W51e2 has been resolved into at least three bright, compact components (see

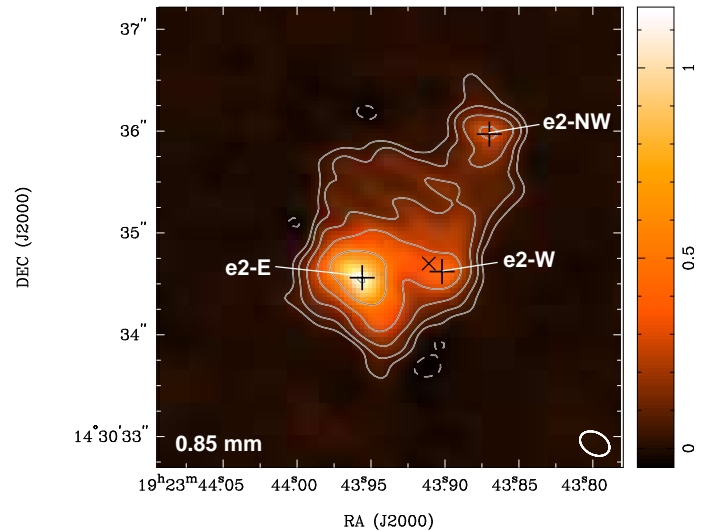


FIG. 1.— High-resolution 0.85 mm continuum image of W51e2 observed with the SMA. Contours are  $\pm 5\sigma \times 2^n$  ( $n = 0, 1, 2, 3, \dots$  and  $\sigma = 7.11 \text{ mJy beam}^{-1}$ ). The FWHM beam ( $0.31'' \times 0.22''$ , P.A.= $60.6^\circ$ ) is shown at bottom right. Three continuum emission components e2-NW, e2-E, and e2-W are marked with “+”. The  $\lambda 3.6 \text{ cm}$  position of the UC HII region in W51e2 Gaume et al. (1993) is marked with “x”.

Figure 1, the symbol “+” marks the positions of the components). The brightest source, W51e2-E, is located  $\sim 0.9''$  east of the UC HII region which is marked with “x” for the peak position at 3.6 cm from Gaume et al. (1993). The secondary bright source, W51e2-W, coincides with the 3.6 cm peak of the UC HII region. The third component, W51e2-NW, is located about  $2''$  northwest of W51e2-E. In addition, these compact emission components appear to be surrounded by an amorphous halo in the continuum emission at 0.85 mm. The three bright continuum sources were also detected in the low-resolution continuum image at 1.3 mm (Figure 2(a)). Moreover, a weak continuum component, W51e2-N, is present  $\sim 2''$  north of W51e2-E.

### 2.2. The VLA continuum images at 7 and 13 mm

The observations of W51e2 at 7 and 13 mm were carried out with the VLA (see the summarized observing parameters in Table 1). We made the calibrations by following the standard data-reduction procedure for VLA data with AIPS<sup>4</sup>. Then, the calibrated visibilities were loaded into the Miriad environment.

<sup>3</sup> <http://www.cfa.harvard.edu/sma/miriad>

<sup>4</sup> <http://www.aips.nrao.edu>

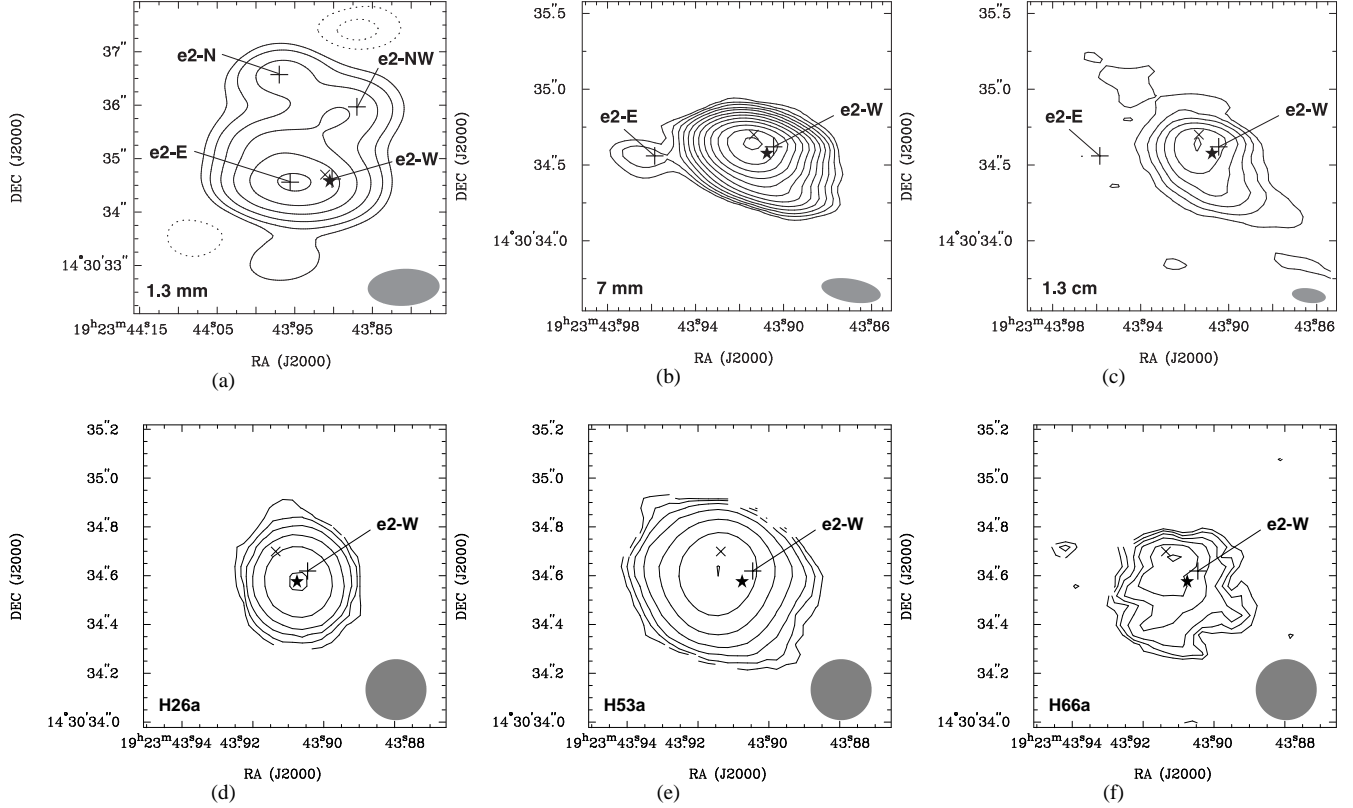


FIG. 2.— (a): 1.3 mm continuum image of W51e2 observed with the SMA. Contours are  $\pm 5\sigma \times 2^n$  ( $n = 0, 1, 2, 3, \dots$  and  $\sigma = 14.0$  mJy beam $^{-1}$ ). The FWHM beam ( $1.35'' \times 0.69''$ , P.A.= $-87.4^\circ$ ) is shown at bottom right. The three components detected at 0.85 mm together with the additional component e2-N detected at 1.3 mm are marked with “+”. The position “+” of the submillimeter components and the peaks of the 3.6 cm continuum (“x”) and H26 $\alpha$  (“★”) are also marked in the rest of the images. (b): 7 mm continuum image of W51e2 observed with the VLA. Contours are  $\pm 5\sigma \times 2^{n/2}$  ( $n = 0, 1, 2, 3, \dots$  and  $\sigma = 1.12$  mJy beam $^{-1}$ ). The FWHM beam ( $0.40'' \times 0.15''$ , P.A.= $80.3^\circ$ ) is shown at bottom-right. (c): 13 mm continuum image of W51e2 observed with VLA. Contours are  $\pm 5\sigma \times 2^n$  ( $n = 0, 1, 2, 3, \dots$  and  $\sigma = 0.50$  mJy beam $^{-1}$ ). The FWHM beam ( $0.23'' \times 0.10''$ , P.A.= $82.6^\circ$ ) is shown at bottom right. (d): Image of the H26 $\alpha$  line emission integrated from 25 km s $^{-1}$  to 84 km s $^{-1}$  from W51e2. Contours are  $\pm 5\sigma \times 2^n$  ( $n = 0, 1, 2, 3, \dots$  and  $\sigma = 0.146$  Jy beam $^{-1}$  km s $^{-1}$ ). The FWHM beam ( $0.25''$ ) is shown at bottom right. All the RRL images are convolved to a common circular beam ( $0.25''$ ). The star denotes the peak position of the H26 $\alpha$  line and is marked in the rest of the RRL images. (e): Image of the H53 $\alpha$  line emission integrated from 22 km s $^{-1}$  to 101 km s $^{-1}$ . Contours are  $\pm 5\sigma \times 2^n$  ( $n = 0, 1, 2, 3, \dots$  and  $\sigma = 9.68 \times 10^{-3}$  Jy beam $^{-1}$  km s $^{-1}$ ). (f): Image of the H66 $\alpha$  line emission integrated from 24 km s $^{-1}$  to 120 km s $^{-1}$ . Contours are  $\pm 5\sigma \times 2^{n/2}$  ( $n = 0, 1, 2, 3, \dots$  and  $\sigma = 6.14 \times 10^{-3}$  Jy beam $^{-1}$  km s $^{-1}$ ).

The imaging and further analysis were carried out with Miriad.

The dirty images were made using INVERT with robust weighting (robust=0) and were cleaned with the hybrid deconvolution algorithm. Figures 2(b) and 2(c) show the continuum images at 7 and 13 mm, respectively. Strong continuum emission is detected from W51e2-W at both 7 and 13 mm in good agreement with previous observations at centimeters (Gaume et al. 1993). In addition, a weak but significant ( $>10\sigma$ ) emission feature at W51e2-E has been detected at only 7 mm. As shown in Figure 2(b), the weak 7 mm continuum source at W51e2-E has been clearly separated from the UC HII region, W51e2-W.

### 2.3. Hydrogen recombination lines

For the line cubes, the continuum emission was subtracted using the linear interpolation from the line-free channels with UVLIN. The H26 $\alpha$  line (353.623 GHz) was included in the line cubes made from the SMA data at 0.85 mm. We also made a line image cube to cover the H30 $\alpha$  line (231.901 GHz) from the SMA data at 1.3 mm. Both the H26 $\alpha$  and H30 $\alpha$  line data were resampled to 1 km s $^{-1}$ . The rms noises of 49 mJy beam $^{-1}$  and 81 mJy beam $^{-1}$  in each of the channel images are inferred for the H26 $\alpha$  and H30 $\alpha$  line image cubes, respectively. Figure 2(d) shows the integrated line intensity image of the H26 $\alpha$  line made

with a  $3\sigma$  cutoff in the velocity range from 25 to 84 km s $^{-1}$ . The H26 $\alpha$  line emission from the UC HII region (W51e2-W) appears to be very compact and has not been resolved with the beam of  $0.25''$ , suggesting that the intrinsic source size of the hyper-compact HII core is  $< 0.06''$ . The peak position of the integrated H26 $\alpha$  line emission (stars in Figure 2) appears to have a significant offset of  $\sim 0.15''$  from the continuum peak at 13 mm (also see the Gaume’s position in Figure 2(d)). Unlike the other RRLs and continuum emission at centimeter wavelengths, the line emission at the frequency of the H30 $\alpha$  line (the image is not shown in this paper) shows an extended distribution covering the entire  $3''$  region, suggesting that the H30 $\alpha$  line might have been severely contaminated by one or more molecular lines in W51e2 (e.g., C $_3$ H $_7$ CN with a rest frequency of 231.9009 GHz).

The line of H66 $\alpha$  is broad and weak, which is barely covered by the VLA correlator band with which we had difficulty determining the line-free channels. Instead, the continuum levels were determined by averaging all channels excluding a few relatively strong line emission channels and were subtracted from the visibility data. The uncertainty is  $< 5\%$  in the continuum levels due to the line contamination. The image cubes of the H53 $\alpha$  and H66 $\alpha$  lines were cleaned and convolved to a circular

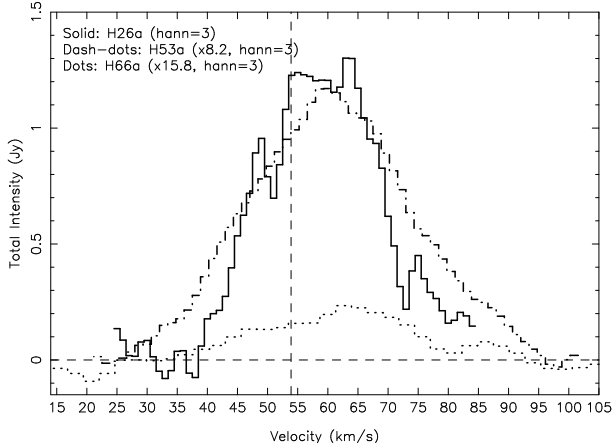


FIG. 3.— Profiles of hydrogen recombination lines, H26 $\alpha$ , H53 $\alpha$ , and H66 $\alpha$ , integrated from W51e2-W in an area of  $0.5'' \times 0.5''$  centered at the H26 $\alpha$  line peak. All the line images have been convolved with the same circular beam of  $0.25''$ . The spectra are multiplied with the ratios of the rest frequency of the H26 $\alpha$  line to the RRL rest frequencies ( $\nu_{H26\alpha}/\nu_{RRL}$ ). The vertical dashed line denotes the systematic velocity of  $53.9 \pm 1.1 \text{ km s}^{-1}$  which we determined from the previous measurements of seven different hot molecular lines (see Section 2.4).

beam of  $0.25''$ , giving the rms noises of 2.4 and 1.5 mJy beam $^{-1}$  per channel, respectively. The integrated intensities of H53 $\alpha$  (with a  $3\sigma$  cutoff in each channel) and H66 $\alpha$  (with a  $2\sigma$  cutoff in each channel) are shown in Figures 2(e) and 2(f), respectively. Both H53 $\alpha$ , and H66 $\alpha$  lines are detected from only W51e2-W, the UC HII region. For the H26 $\alpha$ , H53 $\alpha$ , and H66 $\alpha$  lines from W51e2-W, we integrated the line emission region with a size of  $0.5''$  around the H26 $\alpha$  peak position. The profiles of the H26 $\alpha$ , H53 $\alpha$  and H66 $\alpha$  lines are multiplied by the frequency ratios of  $\nu_{H26\alpha}/\nu_{H26\alpha}$ ,  $\nu_{H26\alpha}/\nu_{H53\alpha}$  and  $\nu_{H26\alpha}/\nu_{H66\alpha}$ , respectively, as shown in Figure 3. The measurements of the peak intensity ( $I_{peak}$ ), radial velocity ( $V_{LSR}$ ), and FWHM line width ( $\Delta V$ ) for the H26 $\alpha$ , H53 $\alpha$ , and H66 $\alpha$  lines are given in Table 3.

#### 2.4. Absorption of HCN(4-3) and CO(2-1)

The systematic velocity of W51e2 varies when it is measured using different hot molecular lines (Sollins et al. 2004; Remijan et al. 2004; Zhang et al. 1998; Rudolph et al. 1990). In order to minimize the possible effects of the different distributions with different molecular lines, we averaged these measurements of molecular lines H $^{13}$ CO $^+$ , SO $_2$ , SiO, CH $_3$ CN, and HCO $^+$  and obtained a mean value of  $53.9 \pm 1.1 \text{ km s}^{-1}$ . We adopt this value as the systematic velocity for W51e2-E hereafter.

The lines of HCN(4-3) at  $\nu_0 = 354.505 \text{ GHz}$  and CO(2-1) at  $\nu_0 = 230.538 \text{ GHz}$  were covered in the SMA observations at 0.85 mm and 1.3 mm, respectively. The dirty images were made with natural weighting and deconvolved with the Hogbom Clark Steer hybrid algorithm. The final rms noises of  $\sigma = 65$  and  $94 \text{ mJy beam}^{-1}$  per channel ( $1 \text{ km s}^{-1}$  in the channel width) were achieved for HCN(4-3) and CO(2-1), respectively. Figure 4 shows the spectra of HCN(4-3) toward W51e2-E and W51e2-W and the spectrum of CO(2-1) near the peak position of W51e2-E. A significant absorption of the HCN(4-3) line is detected against the submillimeter core, W51e2-E, and most of which is redshifted with respect to the systematic velocity of  $53.9 \pm 1.1 \text{ km s}^{-1}$  as indicated by the vertical dashed line in Figure 4(c). Note that the redshifted absorption of HCN observed with the high angular resolution against the compact continuum

core corresponds to the cold gas in front of the dust core moving toward it, i.e., the infall. The CO(2-1) spectrum shows a broader redshifted feature in absorption than that of HCN. Due to the poor angular resolution in the CO(2-1) observations, the observed broad profile in absorption is caused not only by the infall but also by the outflow. In particular, the high redshifted absorption arises very likely from the outflow gas. In comparison with that of W51e2-E, the spectrum toward W51e2-W only shows a weak spectral feature (Figure 4(d)) which can be characterized as an inverse P Cygni profile, suggesting that only little molecular gas (if present) falls onto the UC HII region.

To show the spatial distribution of the absorption gas, we carried out a moment analysis. The calculation of the zeroth moment corresponds to the integrated intensity over the velocity. In order to avoid cancellation between emission and absorption spectral features in the same beam area, we separate the absorption and emission in the moment calculation. We found that both the blueshifted and redshifted emission of the HCN(4-3) line (the images are not shown in this paper) is extended from northwest to southeast across W51e2-E, which is, in general, consistent with the molecular outflow direction as suggested based on the CO(2-1) line observation (Keto & Klaassen 2008). The HCN(4-3) absorption, integrated from 44 to  $62 \text{ km s}^{-1}$  with a  $5\sigma$  cutoff in each channel (Figure 4(a)), is found to be mainly concentrated on W51e2-E. From the lower-resolution observation, the distribution of the CO(2-1) absorption line integrated from 43 to  $71 \text{ km s}^{-1}$  (a  $5\sigma$  cutoff in each channel, see Figure 4(b)), also shows the absorption peaks at W51e2-E instead of W51e2-W. We also note that the CO(2-1) absorption shows a relatively extended feature north of W51e2-E, further indicating that the absorption of CO(2-1) might indeed be significantly contaminated by the outflow gas.

Along with the absorption spectra, the distribution of the absorbing gas in W51e2 evidently demonstrates that the submillimeter (dust) core W51e2-E, instead of W51e2-W (the UC HII region), is the center of accretion for the majority of the high-density gas from this molecular core.

#### 2.5. Spectral Energy Distributions

In lack of high angular resolution observations at millimeter/submillimeter wavelengths, the flux densities from the entire region of W51e2 were considered in the previous analyses of the SED (Rudolph et al. 1990; Sollins et al. 2004; Keto et al. 2008). With the high-resolution observations at the wavelengths from radio to submillimeter, we are now able to spatially separate individual emission components in our SED analysis.

Adding the data at 3.6 cm (Gaume et al. 1993) and at 2 and 6 cm (Rudolph et al. 1990) along with the continuum data at the four wavelengths (13, 7, 1.3, and 0.8 mm) discussed in this paper, we have seven measurements in flux densities covering nearly 2 order of magnitude in frequency. For 13, 7, and 0.8 mm data, the flux density measurements were made by fitting a Gaussian to the individual emission components in the images with the same size of the convolved FWHM beam ( $0.4''$ ). For the 1.3 mm data, we determined the flux density by fitting multiple Gaussian components to the emission features in a relatively lower resolution ( $1.1''$ ), which results in relatively large uncertainties. For the emission cores W51e2-W, W51e2-E, W51e2-NW, and W51e2-N, the flux densities determined are given in Table 2. The relevant continuum spectra for the four emission components are shown in Figure 5.

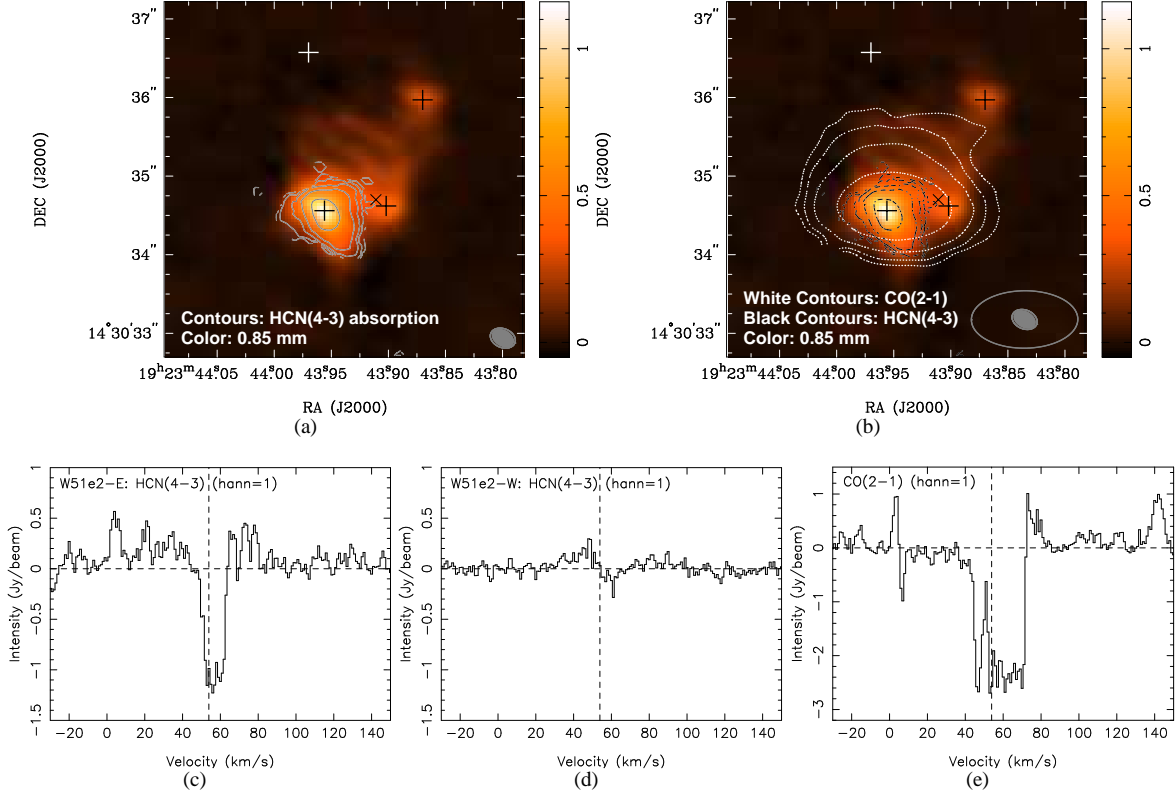


FIG. 4.— (a): Image of the HCN(4-3) absorption line integrated from 44 to 62 km s<sup>-1</sup>. Dashed contours are  $\pm 5\sigma \times 2''$  ( $n = 0, 1, 2, 3, \dots$  and  $\sigma = 0.113$  Jy beam<sup>-1</sup> km s<sup>-1</sup>), overlaid on the gray-scaled continuum image at 0.85 mm. The FWHM beam  $0.33'' \times 0.24''$  (sup=0) is shown at bottom right. (b): Image of the CO(2-1) absorption line integrated from 43 to 71 km s<sup>-1</sup>. White dashed contours are  $\pm 5\sigma \times 2''$  ( $n = 0, 1, 2, 3, \dots$  and  $\sigma = 0.771$  Jy beam<sup>-1</sup> km s<sup>-1</sup>), overlaid on the gray-scaled continuum image at 0.85 mm. The FWHM beam  $1.35'' \times 0.73''$  (sup=0) is shown at bottom right. (c and d): The spectral profiles of the HCN(4-3) absorption line toward W51e2-E and W51e2-W, respectively. The vertical dashed line denotes the systematic velocity of  $53.9 \pm 1.1$  km s<sup>-1</sup>. (e): The spectral profile of the CO(2-1) absorption line toward W51e2-E, with a vertical dashed line for the systematic velocity.

### 3. NATURE OF THE W51E2 COMPLEX

Four distinct components have been identified in the  $3''$  region of W51e2 from the high-resolution images at wavelengths from centimeter to submillimeter (Figure 1 and 2). The nature of these components is discussed as follows.

#### 3.1. W51e2-W: UC HII region

W51e2-W is the only core detected at centimeter wavelengths, and its continuum emission is dominated by the free-free emission from the ionized core and traces the thermal HII region around the central star. Figure 2(b)–(f) show the UC HII region, W51e2-W, including an unresolved core (a possible ionized disk) and a northeast and southwest (NE–SW) extension as a possible outflow. The NE and SW extensions are best to be seen at 7 and 13 mm in Figure 2(b) and (c), which is in good agreement with the previous observations at 3.6 and 1.3 cm by Gaume et al. (1993). Gaume et al. (1993) found the spectral indices  $\alpha$  of about 2 (optically thick) and 0.4 for the NE and SW extensions of W51e2-W, respectively, and suggested that there is a one-side (SW) collimated ionized outflow from the core.

The H26 $\alpha$  line is an excellent tracer for hyper-compact ionized cores (star in Figure 2(d)), providing a good diagnosis for the presence of an ionized disk. On the basis of the SMA observations with an angular resolution of  $0.25''$ , the hyper-compact ionized core which peaked at  $59.1$  km s<sup>-1</sup> in W51e2-W has not been resolved, giving a limit on the intrinsic size of  $\theta_s < 0.06''$  and linear size  $< 310$  AU from a Gaussian fitting. The elongation shown in the H53 $\alpha$  image (Figure 2(e)) agrees

with the radio continuum images observed at 1.3 cm (Figure 2(c) and Gaume et al. 1993), 3.6 cm (Gaume et al. 1993), and 7 mm (Figure 2(b)), suggesting that the NE–SW extension observed in the H53 $\alpha$  line corresponds to the expansion of ionized gas (or outflow). The H66 $\alpha$  line emission also has a similar elongation (Figure 2(f)), with peak intensity near Gaume’s position in the NE and an extension structure in the SW. We also found a significant velocity gradient of the H53 $\alpha$  line in the W51e2-W region, in agreement with what was observed by Keto & Klaassen (2008), redshifted in the SW and blueshifted in the NE. The broad wings of the recombination lines shown in Figure 3 (also in Table 3) corresponding to extended, optically thin emission indicate that it is hard to explain them as an ionized disk. The velocity gradient observed in the H53 $\alpha$  line is more likely produced by an ionized outflow rather than an ionized accretion disk.

We fitted the SED of W51e2-W with a free-free emission model

$$S_\nu = \Omega_s B_\nu(T_e)(1 - e^{-\tau_c}) \quad (\text{Jy}), \quad (1)$$

where  $S_\nu$  is the flux density at frequency  $\nu$ ,  $\Omega_s$  is the solid angle of the source,  $B_\nu(T_e)$  is the Planck function, and  $T_e$  is the electron temperature. The continuum optical depth is expressed by (Mezger & Henderson 1967) as

$$\tau_c = 0.0824 \left(\frac{T_e}{\text{K}}\right)^{-1.35} \left(\frac{\nu}{\text{GHz}}\right)^{-2.1} \left(\frac{\text{EM}}{\text{pc cm}^{-6}}\right) \alpha(\nu, T_e). \quad (2)$$

The emission measure (EM) can be written as

$$\text{EM} = N_e^2 L_{fV}, \quad (3)$$

TABLE 2  
CORE FLUXES OF W51E2 AT CENTIMETER TO SUBMILLIMETER BANDS

parameters	W51e2-W	W51e2-E	W51e2-NW	W51e2-N	References and Beamsize $\Theta$
R.A.(J2000)	19:23:43.90	19:23:43.96	19:23:43.87	19:23:43.97	This paper
Decl.(J2000)	+14:30:34.62	+14:30:34.56	+14:30:35.97	+14:30:36.57	This paper
Deconvolved size (")*	0.45	0.71	0.38	1.24	This paper
S <sub>0.85mm</sub> (Jy)	0.35±0.07	3.30±0.20	0.81±0.34		This paper: $\Theta = 0.4''$
S <sub>1.3mm</sub> (Jy)		2.15±0.12	0.62±0.12	0.73±0.08	This paper: $\Theta = 1.1''$
S <sub>7mm</sub> (Jy)	0.62±0.09	0.04±0.01	< 0.0052	< 0.0052	This paper: $\Theta = 0.4''$
S <sub>1.3cm</sub> (Jy)	0.43±0.03	< 0.004	< 0.004	< 0.004	This paper: $\Theta = 0.4''$ ; Gaume et al. (1993): upper limit
S <sub>2cm</sub> (Jy)	0.21±0.05				Rudolph et al. (1990): $\Theta = 0.4''$
S <sub>3.6cm</sub> (Jy)	0.067±0.004	< 0.001	< 0.001	< 0.001	Gaume et al. (1993): $\Theta = 0.21''$ ; Gaume et al. (1993): upper limit
S <sub>6cm</sub> (Jy)	0.025±0.003	–	–	–	Rudolph et al. (1990): $\Theta = 0.6''$

\*The sizes of e2-W, e2-E, and e2-NW are derived from the 0.85 mm image, and e2-N is from the 1.3 mm image.

where  $N_e$  is the mean electron density,  $L$  is the path length, and  $f_V$  is the volume filling factor. The dimensionless factor  $\alpha(\nu, T_e)$  is the order of unity (Mezger & Henderson 1967). For a homogeneous ionized core, the model can be expressed with two free parameters, namely,  $T_e$  and EM, for the first approximation described above.

The solid curve in Figure 5(a) shows the best fit to the data, suggesting a turnover frequency of  $\nu_0 \approx 27$  GHz. The derived mean values for the physical parameters for the overall HII region,  $T_e=4900 \pm 320$  K and  $EM=(1.3 \pm 0.2) \times 10^9$  pc cm<sup>-6</sup>, are similar to the previous result in Zhang et al. (1998). Thus, the mean electron density of  $N_e \sim 3 \times 10^5$  cm<sup>-3</sup> is inferred on the assumption of  $Lf_V \sim 0.5'' \times 5.1$  kpc.

Both the Lyman continuum flux ( $N_L$ ) and the excitation parameter ( $U$ ) can be derived (Rubin 1968; Panagia 1973; Matsakis et al. 1976) as follows:

$$N_L \gtrsim 7.5 \times 10^{46} \text{s}^{-1} \left( \frac{S_\nu}{\text{Jy}} \right) \left( \frac{D}{\text{kpc}} \right)^2 \left( \frac{\nu}{\text{GHz}} \right)^{0.1} \times \left( \frac{T_e}{10^4 \text{K}} \right)^{-0.45}, \quad (4)$$

$$U = 3.155 \times 10^{-15} \text{pc cm}^{-2} \left( \frac{N_L}{\text{s}^{-1}} \right)^{\frac{1}{3}} \left( \frac{T_e}{10^4 \text{K}} \right)^{\frac{4}{15}}, \quad (5)$$

where  $D$  is the distance to the source. We assumed  $\alpha(\nu, T_e) \sim 1$ . Based on our model fitting, the continuum emission from e2-W becomes optically thin at a frequency  $> 80$  GHz ( $\tau < 0.1$ ), and we obtained  $N_L=3.0 \times 10^{48}$  s<sup>-1</sup> and  $U=37.6$  pc cm<sup>-2</sup>. The inferred Lyman continuum flux requires a massive star equivalent to a zero-age mean-sequence star of type O8 located inside the UC HII region W51e2-W (Panagia 1973), which is consistent with the result of O7.5 in Rudolph et al. (1990). Alternatively, a cluster of B-type stars can also be responsible for the ionization. The total ionized mass within  $0.5''$  of W51e2-W is  $\sim 0.02 M_\odot$ , which agrees with the value derived by Gaume et al. (1993).

For the hyper-compact core ( $\theta_s < 0.06''$ ) as observed with the H26 $\alpha$  line, the electron temperature can be estimated from the H26 $\alpha$  line and the continuum flux density at 354 GHz (0.85 mm) on the assumption of optically thin, LTE condition:

$$T_e^* = \left[ \left( \frac{6985}{\alpha(\nu, T_e)} \right) \left( \frac{\nu}{\text{GHz}} \right)^{1.1} \left( \frac{\Delta V_{\text{H26}\alpha}}{\text{km s}^{-1}} \right)^{-1} \left( \frac{S_{0.85\text{mm}}}{S_{\text{H26}\alpha}} \right) \times \left( \frac{1}{1 + \frac{N(\text{He})}{N(\text{H})}} \right) \right]^{0.87}. \quad (6)$$

Assuming  $N(\text{He})/N(\text{H})=0.096$  (Mehringer 1994) and  $\alpha(\nu, T_e)=1$ , we have  $T_e^* = 12,000 \pm 2,000$  K which appears to be considerably higher than the mean electron temperature of the overall HII region. The EM of the hyper-compact HII core can be assessed as

$$EM = 7.1 \text{ pc cm}^{-6} \left( \frac{T_e}{\text{K}} \right)^{3/2} \left( \frac{\theta_s}{\text{arcsec}} \right)^{-2} \left( \frac{\lambda}{\text{mm}} \right) \left( \frac{S_L}{\text{Jy}} \right) \times \left( \frac{\Delta V}{\text{km s}^{-1}} \right), \quad (7)$$

where  $T_e$  is the electron temperature,  $\theta_s$  is the intrinsic size of the HII region,  $S_L$  is the peak line intensity in Jy,  $\Delta V$  is the FWHM line width in km s<sup>-1</sup>, and  $\lambda$  is the observing wavelength in millimeters. Based on the measurements of the H26 $\alpha$  line from the hyper-compact ionized core together with the assumption of  $T_e \approx T_e^*$ ,  $EM > 7 \times 10^{10}$  pc cm<sup>-6</sup> is found. The corresponding lower limit of the volume electron density is  $N_e > 7 \times 10^6$  cm<sup>-3</sup> assuming  $Lf_V < 0.06'' \times 5.1$  kpc. The inferred high electron temperature and high electron density suggest that the H26 $\alpha$  line arises from a hot, very compact region ( $< 0.06''$ ) which is probably close to the central ionizing star(s). With the nature of optically thin and sensitive to the high-density ionized gas, the H26 $\alpha$  line is an excellent tracer of the hot, high-density ionized region surrounding the ionizing source. In comparison with the mean electron temperature ( $T_e=4900$  K) inferred from the free-free emission in a large area ( $0.5''$ ), the high temperature of  $T_e=12,000$  K derived from the H26 $\alpha$  in a compact area ( $< 0.06''$ ) suggests that a temperature gradient is present along the radius of the UC HII region W51e2-W.

Observations of RRLs in a wide range at wavelengths from centimeters to submillimeters also offer a means to further explore physical conditions of W51e2-W. Table 3 summarizes the reliable measurements of three RRLs from W51e2, namely, H26 $\alpha$ , H53 $\alpha$ , and H66 $\alpha$ . We plotted the spectral profiles of the three RRLs together, and each of the profiles has been multiplied by a factor of  $\nu_{26\alpha}/\nu_{n\alpha}$ , the ratio of the H26 $\alpha$  line frequency to that of RRLs (Figure 3). In the case of optically thin and no-pressure broadening, the three line profiles should match each other. Comparing H53 $\alpha$  with H26 $\alpha$ , we find that the peak intensities of the two lines agree with each other, which suggests that, in general, both the H53 $\alpha$  and H26 $\alpha$  lines are under an optically thin, LTE condition. Several velocity peaks in the H26 $\alpha$  line indicate multiple kinematic components in the hyper-compact HII core. The H53 $\alpha$  line is characterized by a relatively smooth profile with large velocity wings. The large

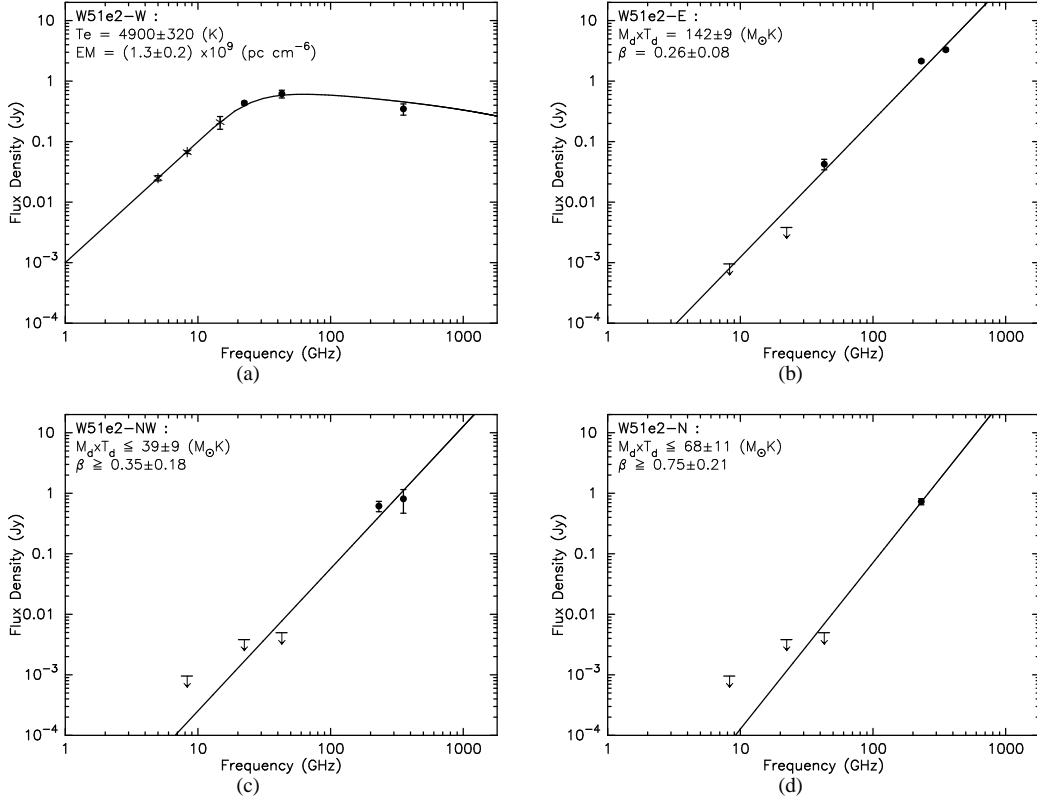


FIG. 5.— The SED for W51e2 cores. (a): SED fitting for W51e2-W with a free-free emission model. Black points denote the measurements from this work, and the asterisks are from Rudolph et al. (1990) and Gaume et al. (1993). All flux values are listed in Table 2. The arrows denote the upper limits from Rudolph et al. (1990) and Gaume et al. (1993). (c): The SED fitting for the W51e2-NW core. The upper limit of the flux density at 43 GHz (7 mm) is from our data ( $3\sigma$  of the 7 mm image). (d): The SED fitting for the W51e2-N core.

velocity wings observed in the H53 $\alpha$  line can be explained by the large velocity gradient in the lower-density electron gas of the ionized outflow (Gaume et al. 1993). However, the line intensity of H66 $\alpha$  appears to be significantly weaker than the other two high-frequency RRLs. The peak of the modified line profile of H66 $\alpha$  is a factor of  $\sim 5$  less than that of the other two. Considering the fact that the frequency of H66 $\alpha$  is below the turnover frequency of  $\nu_0 \approx 27$  GHz, we found that the H66 $\alpha$  line from the ionized gas is obscured severely due to the self-absorption process in the hyper-compact HII core. From Equation (2), a mean optical depth of  $\tau_c = 1.6$  at  $\nu_{H66\alpha} = 22.36$  GHz is found. The exponential attenuation of  $\exp(-1.6) \approx 0.2$  suggests that the H66 $\alpha$  line is attenuated mainly due to the self-absorption in the ionized core. In addition, the pressure broadening effect which weakens the lower frequency lines needs to be assessed.

The total line width of RRLs ( $\Delta V$ ) can be expressed by the Doppler broadening ( $\Delta V_D$ ) and pressure broadening ( $\Delta V_P$ ). According to Brocklehurst & Leeman (1971) and Gordon & Sorochenkova (2002), we have

$$\Delta V_D = \text{km s}^{-1} \sqrt{0.0458 \times \left(\frac{T_e}{\text{K}}\right) + \left(\frac{\Delta V_t}{\text{km s}^{-1}}\right)^2}, \quad (8)$$

$$\Delta V_P = 3.74 \times 10^{-14} \text{ km s}^{-1} n^{4.4} \left(\frac{\lambda}{\text{mm}}\right) \left(\frac{N_e}{\text{cm}^{-3}}\right) \times \left(\frac{T_e}{\text{K}}\right)^{-0.1}, \quad (9)$$

$$\Delta V = \sqrt{\Delta V_D^2 + \Delta V_P^2}, \quad (10)$$

TABLE 3  
PARAMETERS OF RRLS DERIVED FROM OUR DATA\*

	H26 $\alpha$	H53 $\alpha$	H66 $\alpha$
Rest Frequency (GHz)	353.623	42.952	22.364
Measurements			
$I_{\text{peak}}$ (Jy)	1.29 $\pm$ 0.02	0.137 $\pm$ 0.001	0.015 $\pm$ 0.003
$V_{\text{LSR}}$ (km s $^{-1}$ )	59.1 $\pm$ 0.2	60.4 $\pm$ 0.2	62.1 $\pm$ 1.3
$\Delta V$ (km s $^{-1}$ )	23.1 $\pm$ 0.5	32.0 $\pm$ 0.3	35.1 $\pm$ 8.3
Derived line broadenings			
$\Delta V_P$ (km s $^{-1}$ )	0.01	1.3	6.5
$\Delta V_T$ (km s $^{-1}$ )	15.0	15.0	15.0
$\Delta V_i$ (km s $^{-1}$ )	17.5	28.3	31.1
$\Delta V_D$ (km s $^{-1}$ )	23.1	32.0	34.5

\*All line profiles are integrated from the  $0.5'' \times 0.5''$  region around the peak position of H26 $\alpha$  from maps of the same beamsize of  $0.25''$ .

$\Delta V_t$  is the turbulent broadening of the gas including broadening due to outflows and disk rotations and  $n$  is the principal quantum number of the transition. We calculated broadenings on the mean electron temperature ( $T_e \approx 4900$  K) and the mean electron density ( $N_e \approx 3 \times 10^5 \text{ cm}^{-3}$ ) of the UC HII region. The thermal broadening ( $\Delta V_T$ ) is 15 km s $^{-1}$  for  $T_e = 4900$  K. The pressure broadening is a strong function of the principal quantum number, i.e.,  $\Delta V_P$  increases drastically toward the low-frequency lines. For the high-frequency line (H26 $\alpha$ ), the pressure broadening ( $\Delta V_P = 0.01 \text{ km s}^{-1}$ ) can be ignored, while for the H66 $\alpha$  line, the pressure broadening of  $\Delta V_P = 7 \text{ km s}^{-1}$  becomes significant. The pressure broadening is  $\Delta V_P = 76 \text{ km s}^{-1}$

for the H92 $\alpha$  line, which can actually wash out the profile of the line emission. Thus, in addition to the opacity effect, the pressure broadening may also make a considerable contribution to diminish the H92 $\alpha$  line which was not detected in the observations of Mehringer (1994). The turbulent and/or the dynamical motions of the ionized gas contribute a total of  $\Delta V_i \approx 18 \text{ km s}^{-1}$  in the line broadening for the H26 $\alpha$  line and  $\Delta V_i \approx 28$  and  $31 \text{ km s}^{-1}$  for the H53 $\alpha$  and H66 $\alpha$  lines, respectively. The H26 $\alpha$  line traces the high-density ionized gas in the hyper-compact core or the ionized disk (if it exists) and is less sensitive to the lower-density outflow which produces the broad wings in the line profiles. The turbulent and/or dynamical broadening becomes dominant in the H53 $\alpha$  and H66 $\alpha$  lines, and these lower frequency RRLs (H53 $\alpha$  and H66 $\alpha$ ) better trace the lower-density electron gas in the ionized outflow.

In short, W51e2-W consists of a hyper-compact HII core ( $< 310 \text{ AU}$ ) with an emission measure of  $\text{EM} > 7 \times 10^{10} \text{ pc cm}^{-6}$  and an ionized outflow. An early-type star equivalent to an O8 star (or a cluster of B-type stars) is postulated to have formed within the hyper-compact HII core. The broadening of the line profiles is dominated by the Doppler broadening including both thermal and turbulence/dynamical motions. Pressure broadening becomes significant only for the H66 $\alpha$  line and the lines with a larger principal quantum number.

### 3.2. W51e2-E: A massive proto-stellar core

W51e2-E is located  $\sim 0.9''$  east of the UC HII region W51e2-W. It is the brightest source in the 0.85 mm continuum image (Figure 1). The flux density drops drastically at 7 mm (Figure 2(b)). It cannot be detected at longer wavelengths. The SED of the continuum emission from W51e2-E (Figure 5(b)) appears to arise from a dust core associated with proto-stars.

With the Rayleigh-Jeans approximation, the continuum flux density from a homogeneous, isothermal dust core can be described as (Launhardt & Henning 1997)

$$S_d(\nu) = 6.41 \times 10^{-6} \text{ Jy} \left( \frac{\kappa_0}{\text{cm}^2 \text{g}^{-1}} \right) \left( \frac{\nu}{\nu_0} \right)^\beta \left( \frac{\nu}{\text{GHz}} \right)^2 \times \left( \frac{M_d}{M_\odot} \right) \left( \frac{T_d}{\text{K}} \right) \left( \frac{D}{\text{kpc}} \right)^{-2}, \quad (11)$$

where  $\kappa_0$  is the dust opacity at frequency  $\nu_0$ ,  $\beta$  is the power-law index of the dust emissivity,  $M_d$  is the mass of dust,  $T_d$  is the dust temperature in K, and  $D$  is the distance to the source. We adopt the dust opacity value of  $\kappa(\lambda = 1.3 \text{ mm}) = 0.8 \text{ cm}^2 \text{g}^{-1}$  (Ossenkopf & Henning 1994; Launhardt & Henning 1997) and have three free parameters for the dust core ( $M_d$ ,  $T_d$ , and  $\beta$ ).

The solid line in Figure 5(b) shows the best least-squares fitting to the observed data. The index of  $\beta = 0.26 \pm 0.08$  derived from our fitting indicates that emission from the e2-E core might be dominated by large grains of dust (Miyake & Nakagawa 1993; Chen et al. 1995; Andrews & Williams 2007). In addition, because of a lack of flux density measurements at higher frequencies or shorter wavelengths, the dust mass and temperature are degenerate in our best fitting, i.e.,  $M_d T_d = 142 \pm 9 M_\odot \text{ K}$ . Remijan et al. (2004) derived the kinetic temperature in W51e2 to be  $153 \pm 21 \text{ K}$  from the high-resolution observations of CH<sub>3</sub>CN, which is close to the dust temperature  $T_d = 100 \text{ K}$  used in Zhang et al. (1998). Adopting that  $T_d = 100 \text{ K}$  and assuming that the ratio of H<sub>2</sub> gas to dust is 100, we found that the total mass of  $\sim 140 M_\odot$  is in the W51e2-E core. Emission from the W51e2-E region has been slightly resolved, so that the dust core of W51e2-E might host a number of proto-stellar cores which accrete the

surrounding molecular gas as indicated by both the HCN and CO absorption lines (see Section 2.4). This proposed scenario for W51e2-E is also consistent with the hourglass-like magnetic fields inferred from polarization measurements of Tang et al. (2009) for the W51e2 region. The configuration center of  $B$  vectors coincides with the peak position of the W51e2-E dust core.

From a Gaussian fitting to the absorption spectrum of the HCN(4-3) toward the center of W51e2-E (Figure 4(c)), we determined the peak line intensity  $\Delta I_L = -1.3 \pm 0.1 \text{ Jy beam}^{-1}$ , the line center velocity  $V_{\text{HCN}} = 56.4 \pm 0.2 \text{ km s}^{-1}$  and the line width of  $\Delta V_{\text{HCN}} = 9.5 \pm 0.4 \text{ km s}^{-1}$ . The infall velocity of the gas is the offset between the center velocity and the systematic velocity, i.e.,  $V_{\text{in}} = V_{\text{HCN}} - V_{\text{sys}} \approx 2.5 \text{ km s}^{-1}$ . The peak continuum intensity of W51e2-E at 0.85 mm is  $I_C = 1.2 \pm 0.01 \text{ Jy beam}^{-1}$  (corresponding to a brightness temperature of  $144 \pm 1 \text{ K}$ ). The ratio of  $-\Delta I_L / I_C \sim 1$  suggests that the absorption line is saturated. Thus, a lower limit on the optical depth (see Qin et al. 2008) is  $\tau_{\text{HCN}} > 3$ . Assuming that the excitation temperature of HCN(4-3) equals the dust temperature, 100 K, we obtained a lower limit of HCN column density of  $7.9 \times 10^{15} \text{ cm}^{-2}$ . Taking  $[H_2]/[HCN] \sim 0.5 \times 10^8$  (Irvine et al. 1987) and the size of the infall region as  $0.75''$  ( $\sim 4000 \text{ AU}$ , see Figure 4(a)), we found that the hydrogen volume density  $N_{\text{H}_2} \sim 6.9 \times 10^6 \text{ cm}^{-3}$ . The infall rate of the gas can be estimated by

$$dM/dt = 2.1 \times 10^{-5} M_\odot \text{ yr}^{-1} \left( \frac{\theta_{\text{in}}}{\text{arcsec}} \right)^2 \left( \frac{D}{\text{kpc}} \right)^2 \left( \frac{V_{\text{in}}}{\text{km s}^{-1}} \right) \times \left( \frac{N_{\text{H}_2}}{10^6 \text{ cm}^{-3}} \right), \quad (12)$$

where  $2\theta_{\text{in}} = 0.75''$  is the diameter of the infalling region,  $D$  is the distance to the source,  $V_{\text{in}}$  is the infall velocity, and the molecular mass ratio  $m/m_{\text{H}_2} = 1.36$  is assumed. With the derived parameters a lower limit of infall rate  $1.3 \times 10^{-3} M_\odot \text{ yr}^{-1}$  is inferred, suggesting that W51e2-E is the accretion center of the W51e2 complex.

### 3.3. W51e2-NW and W51e2-N

W51e2-NW was clearly detected by Tang et al. (2009) in the continuum emission at 0.87 mm. They also found a significant concentration of  $B$  fields at the e2-NW. Genzel et al. (1981) and Imai et al. (2002) detected bright and compact H<sub>2</sub>O masers near this source. We also detected local enhanced continuum emission at 0.85 and 1.3 mm. No significant continuum emission has been detected at 7 and 13 mm (Figure 1 and 2), and there are no significant absorption lines of HCN(4-3) and CO(2-1) in this region. We fitted the SED of continuum emission with a thermal dust model as shown in Figure 5(c). A lower limit of  $\beta \geq 0.35$  is derived from the fitting, which leads to an upper limit of  $M_d T_d \leq 39 M_\odot \text{ K}$ . Assuming the dust temperature in this region to be  $\sim 100 \text{ K}$ , we inferred an upper limit of  $40 M_\odot$  in the total gas mass if the ratio of H<sub>2</sub> gas to dust is equal to 100. W51e2-NW appears to be a massive core at a very early phase of star formation.

Located  $\sim 2''$  north from W51e2-E, W51e2-N is detected in continuum emission from our lower-resolution ( $1.4'' \times 0.7''$ ) image at 1.3 mm (Figure 2(a)). This source appears to be resolved out with a high angular resolution ( $0.3'' \times 0.2''$ ) observation at 0.85 mm. No significant continuum emission was detected at the longer wavelengths. The SED consisting of the flux density at 1.3 mm and the upper limits at 7, 13, and 36 mm is also fitted with a thermal dust model. From the fitted values of the parameters  $\beta \geq 0.75$  and  $M_d T_d \leq 68 M_\odot \text{ K}$ , we found



an upper limit of  $M_d \lesssim 70 M_\odot$  if  $T_d \sim 100$  K and the  $H_2$  gas to dust ratio is 100. No maser activities have been detected from W51e2-N, suggesting that W51e2-N is probably a primordial molecular clump in W51e2.

### 3.4. A propagating scenario of star formation in W51e2

Apparently, in the massive molecular core W51e2, the gravitational collapse occurred first at W51e2-W where an O8 star or a cluster of B-type stars were formed. Based on the absorption spectrum of the HCN line, there appears to be little molecular gas present in the immediate environs. The accretion appears to be paused by the intensive radiation pressure from the central ionized star(s). Most of the surrounding gas ( $\sim 0.02 M_\odot$ ) has been ionized. The thermal pressure in the UC HII region drives an ionized outflow from the ionized core. The submillimeter observations of dust emission and molecular line absorption show that the major accretion now has been re-directed to W51e2-E,  $0.9''$  ( $\sim 4600$  AU) east from W51e2-W. W51e2-E becomes the new dominant gravitational center accreting mass from the surroundings with a rate of  $10^{-3} M_\odot \text{ yr}^{-1}$ . Star formation activities take place in this massive core, as shown by maser activities, outflow, and organized *B*-field structure. Since no free-free emission and no RRLs have been detected, the massive core W51e2-E likely hosts one or more massive protostars. The offset of the radial velocities between the two cores, W51e2-E and W51e2-W, is  $\delta V = 59.1 - 53.9 = 5.2 \text{ km s}^{-1}$ . If W51e2-W and W51e2-E are gravitationally bound and W51e2-W is circularly orbiting around W51e2-E, W51e2-W has a dynamical mass of  $> 140 M_\odot$ , in good agreement with the mass derived from the SED analysis.

A bipolar outflow from W51e2-E has been suggested from the observations of molecular lines. The impact of the outflow on the medium in its path may trigger the collapse of the sub-core W51e2-NW and induce further star formation activities there. W51e2-N represents a gas clump with a considerable amount of mass for the star formation. This speculative scenario appears to reasonably explain what we have observed in the W51e2 complex.

## 4. SUMMARY AND CONCLUSIONS

We have presented high-resolution images of the W51e2 region at 0.85, 1.3, 7, and 13 mm for continuum and hydrogen recombination lines ( $H_{26\alpha}$ ,  $H_{53\alpha}$ , and  $H_{66\alpha}$ ) and the molecular lines (HCN(4-3) and CO(2-1)). The W51e2 complex has been resolved into four distinct components, W51e2-W, W51e2-E, W51e2-NW, and W51e2-N. We have carried out a comprehensive analysis of the continuum SED, the RRLs, and the molecular absorption lines and found that the four cores are at different phases of massive star formation.

1. W51e2-W, associated with the UC HII region, is the only source from which the  $H_{26\alpha}$ ,  $H_{53\alpha}$ , and  $H_{66\alpha}$  lines have been detected. The Lyman continuum flux inferred from the SED analysis suggests that a massive O8 star or a cluster of B-type stars have been formed within the HII region. The unresolved  $H_{26\alpha}$  line emission region suggests the presence of a hot ( $T_e^* = 12,000 \pm 2,000$  K), hyper-compact ionized core with a velocity of  $59.1 \pm 0.2 \text{ km s}^{-1}$ , a linear size of  $< 310$  AU, and a large emission measure  $EM > 7 \times 10^{10} \text{ pc cm}^{-6}$  (or a high density  $N_e > 7 \times 10^6 \text{ cm}^{-3}$ ). The  $H_{53\alpha}$  and  $H_{66\alpha}$  line images show an SW elongation from the hyper-compact ionized core, suggesting either an expansion or an outflow of the ionized gas with relatively lower density. No significant detection of the

HCN molecular line in absorption against the compact HII region indicates that the significant accretion onto this core has been stopped. The line ratios between the  $H_{26\alpha}$ ,  $H_{53\alpha}$ , and  $H_{66\alpha}$  show that both the  $H_{26\alpha}$  and  $H_{53\alpha}$  lines from W51e2-W are in an optically thin, LTE condition. The emission of the  $H_{66\alpha}$  line from the hyper-compact core appears to be attenuated mainly due to the self-absorption in this HII region. The line profile of the  $H_{26\alpha}$  appears to be dominated by the Doppler broadening due to the thermal motions of the hot electrons while the line broadening in both the  $H_{53\alpha}$  and  $H_{66\alpha}$  is dominated by the Doppler effect due to the dynamical motions of the ionized outflow. The pressure broadening in both the  $H_{26\alpha}$  and  $H_{53\alpha}$  lines is negligible and becomes significant for the  $H_{66\alpha}$  line corresponding to  $\Delta V_P \sim 7 \text{ km s}^{-1}$ .

2. W51e2-E is a massive ( $\sim 140 M_\odot$ ) dust core as suggested based on the SED analysis. No hydrogen recombination lines and no radio continuum emission ( $\lambda > 1 \text{ cm}$ ) have been detected from this region, which suggests that W51e2-E is the major core hosting massive proto-stellar objects. Both the absorptions of HCN(4-3) and CO(2-1) are redshifted with respect to the systematic velocity,  $53.9 \pm 1.1 \text{ km s}^{-1}$ , indicating that a large amount of molecular gas moves toward the massive core. From the ratios of the absorption line to continuum, a large infall rate of  $> 1.3 \times 10^{-3} M_\odot \text{ yr}^{-1}$  is inferred from the HCN absorption line, corresponding to the accretion radius of 2000 AU.

3. W51e2-NW appears to be a massive ( $\lesssim 40 M_\odot$ ) core at an earlier phase of star formation. Given its location in the projected path of the molecular outflow from W51e2-E, the star formation activities of W51e2-NW are likely to be triggered by the outflow impact on the medium in the W51e2 complex.

4. W51e2-N appears to be a relatively less dense but massive clump ( $\lesssim 70 M_\odot$ ) from which no obvious evidence has been found for star formation activities.

We thank the referee for helpful comments, Dr. S.-L. Qin for providing help with the data reduction and analysis, and Professor Y.-F. Wu for helpful discussions. H. Shi and J.-L. Han are supported by the National Natural Science Foundation (NNSF) of China (10773016, 10821061, and 10833003) and the National Key Basic Research Science Foundation of China (2007CB815403).

## REFERENCES

- Andrews, S. M. & Williams, J. P. 2007, *ApJ*, 659, 705  
 Brocklehurst, M. & Leeman, S. 1971, *Astrophys. Lett.*, 9, 35  
 Chen, H., Zhao, J.-H., & Ohashi, N. 1995, *ApJ*, 450, L71+  
 Fish, V. L. & Reid, M. J. 2007, *ApJ*, 670, 1159  
 Gaume, R. A., Johnston, K. J., & Wilson, T. L. 1993, *ApJ*, 417, 645  
 Genzel, R., Becklin, E. E., Moran, J. M., Reid, M. J., Jaffe, D. T., Downes, D., & Wynn-Williams, C. G. 1982, *ApJ*, 255, 527  
 Genzel, R., Downes, D., Schneps, M. H., Reid, M. J., Moran, J. M., Kogan, L. R., Kostenko, V. I., Matveenko, L. I., & Ronnang, B. 1981, *ApJ*, 247, 1039  
 Gordon, M. A. & Sorochenko, R. L., eds. 2002, *Astrophysics and Space Science Library*, Vol. 282, *Radio Recombination Lines. Their Physics and Astronomical Applications*  
 Ho, P. T. P. & Young, L. M. 1996, *ApJ*, 472, 742  
 Imai, H., Watanabe, T., Omodaka, T., Nishio, M., Kameya, O., Miyaji, T., & Nakajima, J. 2002, *PASJ*, 54, 741  
 Irvine, W. M., Goldsmith, P. F., & Hjalmarson, A. 1987, in *Astrophysics and Space Science Library*, Vol. 134, *Interstellar Processes*, ed. D. J. Hollenbach & H. A. Thronson, Jr., 561–609  
 Keto, E. & Klaassen, P. 2008, *ApJ*, 678, L109  
 Keto, E., Zhang, Q., & Kurtz, S. 2008, *ApJ*, 672, 423  
 Kundu, M. R. & Velusamy, T. 1967, *Annales d'Astrophysique*, 30, 59  
 Launhardt, R. & Henning, T. 1997, *A&A*, 326, 329

- Martin, A. H. M. 1972, MNRAS, 157, 31  
Matsakis, D. N., Evans, II, N. J., Sato, T., & Zuckerman, B. 1976, AJ, 81, 172  
Mehringer, D. M. 1994, ApJS, 91, 713  
Mezger, P. G. & Henderson, A. P. 1967, ApJ, 147, 471  
Miyake, K. & Nakagawa, Y. 1993, Icarus, 106, 20  
Ossenkopf, V. & Henning, T. 1994, A&A, 291, 943  
Panagia, N. 1973, AJ, 78, 929  
Qin, S.-L., Zhao, J.-H., Moran, J. M., Marrone, D. P., Patel, N. A., Wang, J.-J., Liu, S.-Y., & Kuan, Y.-J. 2008, ApJ, 677, 353  
Remijan, A., Sutton, E. C., Snyder, L. E., Friedel, D. N., Liu, S.-Y., & Pei, C.-C. 2004, ApJ, 606, 917  
Rubin, R. H. 1968, ApJ, 154, 391  
Rudolph, A., Welch, W. J., Palmer, P., & Dubrulle, B. 1990, ApJ, 363, 528  
Sault, R. J., Teuben, P. J., & Wright, M. C. H. 1995, in Astronomical Society of the Pacific Conference Series, Vol. 77, Astronomical Data Analysis Software and Systems IV, ed. R. A. Shaw, H. E. Payne, & J. J. E. Hayes, 433–+  
Scott, P. F. 1978, MNRAS, 183, 435  
Sollins, P. K., Zhang, Q., & Ho, P. T. P. 2004, ApJ, 606, 943  
Tang, Y., Ho, P. T. P., Koch, P. M., Girart, J. M., Lai, S., & Rao, R. 2009, ApJ, 700, 251  
Westerhout, G. 1958, Bull. Astron. Inst. Netherlands, 14, 215  
Xu, Y., Reid, M. J., Menten, K. M., Brunthaler, A., Zheng, X. W., & Moscadelli, L. 2009, ApJ, 693, 413  
Young, L. M., Keto, E., & Ho, P. T. P. 1998, ApJ, 507, 270  
Zhang, Q. & Ho, P. T. P. 1997, ApJ, 488, 241  
Zhang, Q., Ho, P. T. P., & Ohashi, N. 1998, ApJ, 494, 636